NASA Contractor Report 172275

ICASE

NASA-CR-172275
19840005425

EMBEDDED CAVITY DRAG IN STEADY AND UNSTEADY FLOWS

FOR REFERENCE

NOT TO BE TAKEN FROM THIS ROOM

T. B. Gatski

and

C. E. Grosch

INSTITUTE FOR COMPUTER APPLICATIONS IN SCIENCE AND ENGINEERING
NASA Langley Research Center, Hampton, Virginia 23665

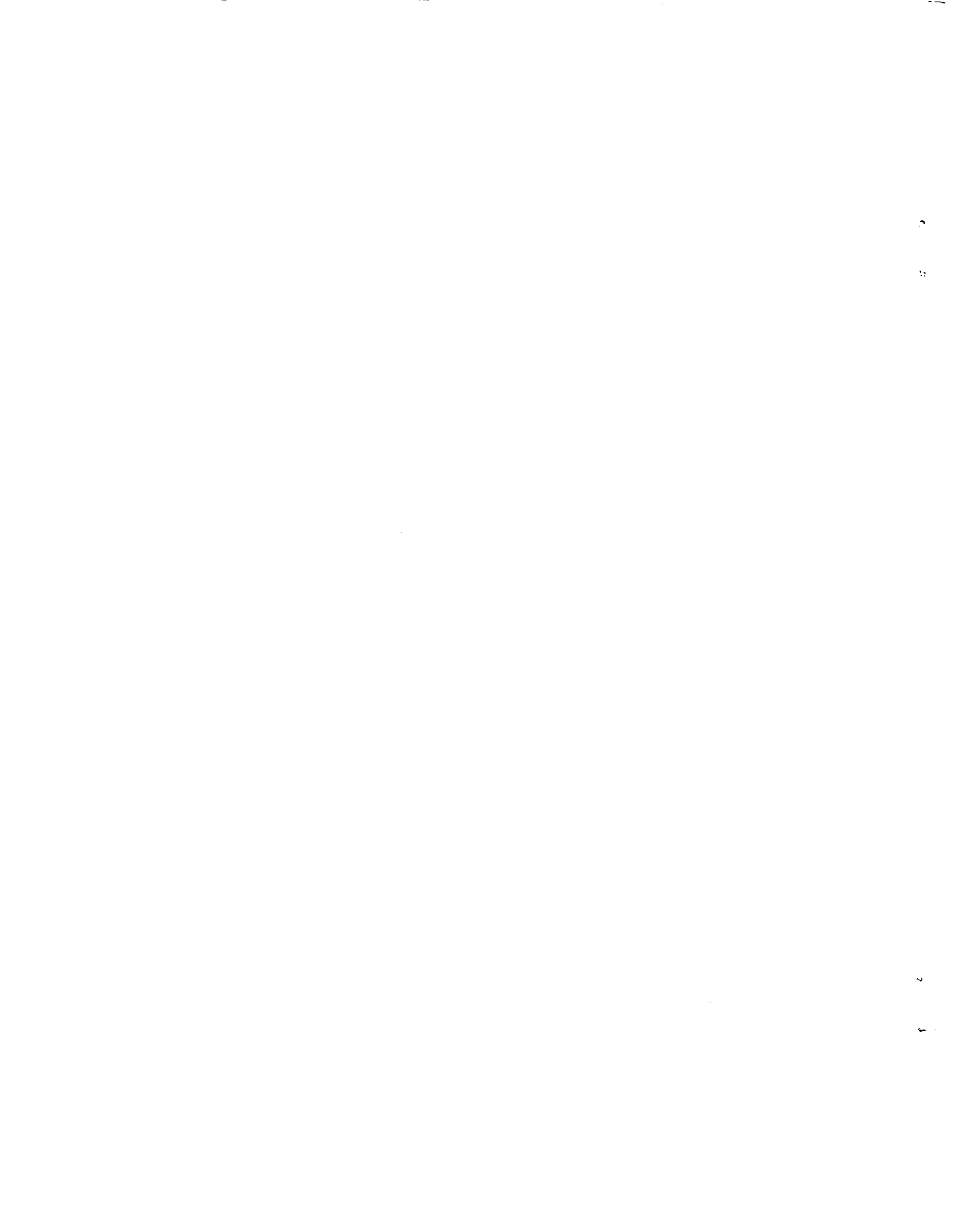Operated by the Universities Space Research Association

NASA

National Aeronautics and
Space Administration

Langley Research Center
Hampton, Virginia 23665

Embedded Cavity Drag in Steady and Unsteady Flows

T. B. Gatski
NASA Langley Research Center

and

C. E. Grosch[*]
Institute for Computer Applications in Science and Engineering
and
Old Dominion University

Abstract

The numerical solution of the laminar boundary-layer flow over an embedded cavity is studied. The purpose of the study is to examine the relevant drag characteristics of laminar cavity flow. The solution field is obtained in terms of velocity and vorticity variables, with the stream function and pressure derivable from the directly computed variables. An analysis and comparison is made among four square cavities, ranging in size from 0.25 to 1.00 boundary-layer thicknesses deep. The dominant flow features are examined in the vicinity of the cavity by means of the stream function and iso-vorticity contours. The dominant physics in the overall drag characteristics of the flow is examined by an analysis of the pressure and wall shear stress distributions in the cavity, and upstream and downstream of the cavity. Pressure forces and frictional forces in, and in the vicinity of, the cavity are determined. Stress relaxation distances, both upstream and downstream of the cavity, are calculated and analyzed. The flow dynamics of the boundary-layer flow over an embedded cavity is summarized. Finally, the relevance of the present results to the control of flow separation in such flows is discussed.

i

N84-13493#
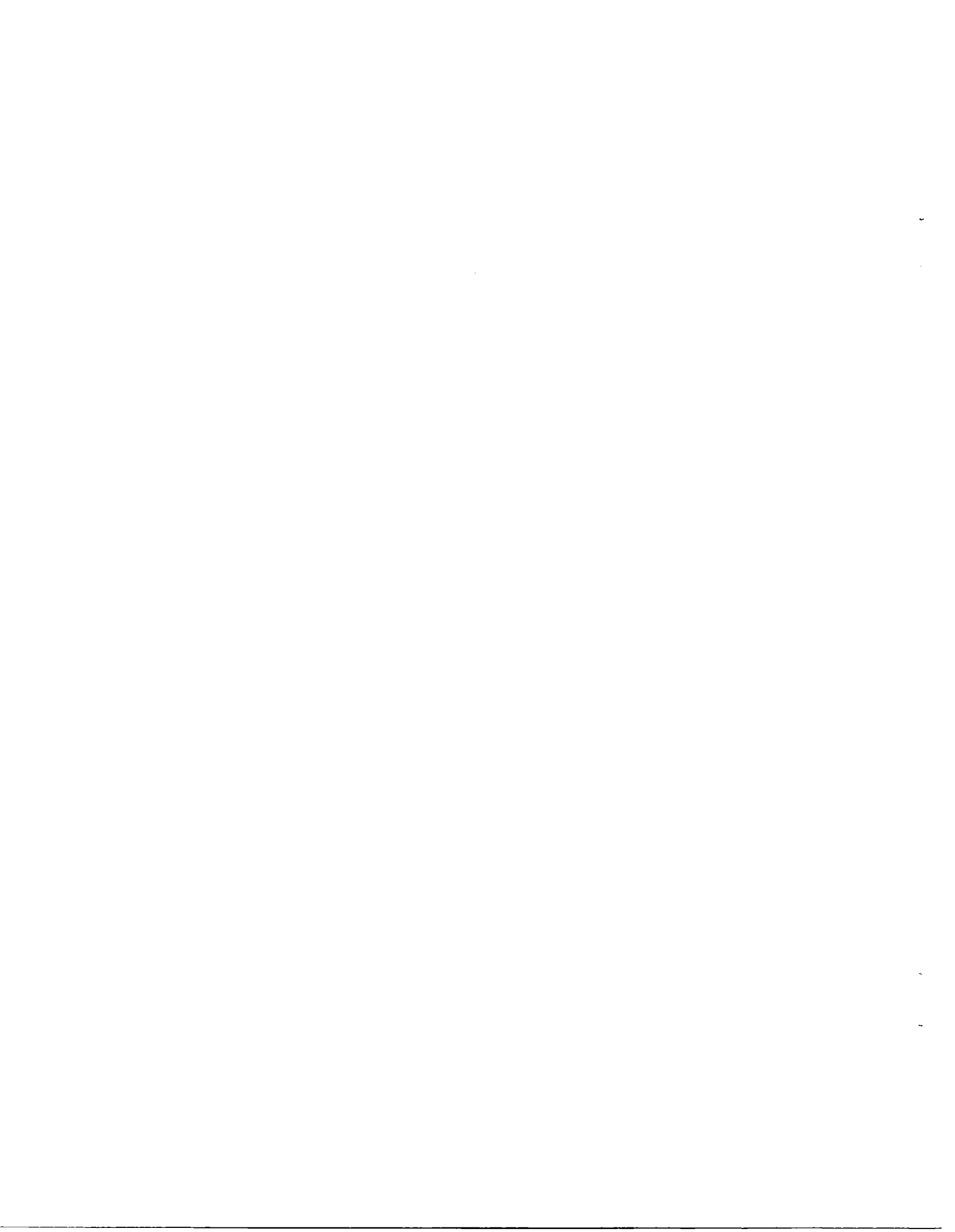
Introduction

A distribution of roughness elements along an otherwise smooth wall bounding surface can significantly alter the dynamic processes of the flow. Such an alteration causes no change in the surface drag along these surfaces in a laminar flow; however, in a turbulent flow there is an increase in the surface drag. It is, of course, necessary to understand the dynamic mechanisms of such surface flows, both laminar and turbulent, so that effective drag controlling measures can be implemented. In the turbulent case, the flow-surface interaction is rather complex due to the broad spectrum of dynamically relevant scales of motion present in the flow. Initially, it is advantageous to treat a more tractable flow situation which incorporates the important parameters and features of the flow. The two-dimensional laminar boundary-layer flow over an embedded cavity constitutes such an initial approximation, and the purpose of this study is to gain further insight into the dynamics of such flows.

There have been several experimental studies of boundary-layer flows over embedded cavities (e.g. Refs. 1-6). Several of these studies, which were mostly for turbulent boundary-layer flows, concentrated on the overall features of the flow, such as velocity and surface pressure distributions as well as skin friction variations: other studies concentrated on more dynamic features of the flow, such as interfacial stability characteristics. There have also been numerical studies on the shear flow driven cavity problem (e.g. Refs. 7-8). These numerical studies have been limited to high-speed flows and do not provide the insight required in the present case. The intent here is to provide flow characteristic information over a range of cavity sizes in a relatively low-speed near-wall environment, which is typical of the local conditions for roughness elements.

The numerical algorithm is a compact difference scheme expressed in terms of the vorticity and velocity (Ref. 9). This work and that appearing in Ref. 10 are applications of the algorithm development presented in Ref. 9 and serve as verification and extensions of the method while also aiding the understanding of the flow dynamics. The compact nature of the algorithm allows for unequally sized computational cells to be easily placed in regions where high resolution is necessary. This aspect of the formulation is important, especially when shear stress and wall-pressure distributions are required. Another important feature of the algorithm is the fact that the dependent variables used in the calculations are interpreted as average values over each edge of the cell. Since these variables are defined at the center of each edge, the corner problem at the upstream and downstream sides of the cavity can be handled in an unambiguous manner. Thus, the pressure induced forces on the vertical walls of the cavity which are critical in the overall drag characteristics, are accurately computed. Finally, wall shear stress, or friction velocity, values are easily extracted from the computed results, as well as other derivable flow variables such as stream function. In addition, velocity profiles and vorticity contour maps in the vicinity of the cavity can be generated to allow for a detailed study of the flow dynamics. The present paper discusses the physical characteristics of the flow in the vicinity of the cavity. Dominant flow features are identified along with a discussion of the possible application of such flow embedded cavities to the control and delay of flow separation.

Mathematical and Numerical Formulation

The problem considered is the incompressible two-dimensional laminar boundary-layer flow over an embedded cavity (see Fig. 1). The governing differential equations for this flow can be written in terms of the velocity and vorticity as

$$\frac{\partial u}{\partial x} + \frac{\partial v}{\partial y} = 0 \tag{1}$$

$$\frac{\partial v}{\partial x} - \frac{\partial u}{\partial y} = \zeta \tag{2}$$

$$\frac{\partial \zeta}{\partial t} + u \frac{\partial \zeta}{\partial x} + v \frac{\partial \zeta}{\partial y} = \frac{1}{R} \nabla^2 \zeta \tag{3}$$

where u and v are the nondimensional streamwise and normal velocity components, respectively, ζ is the nondimensional vorticity, and $R = \dfrac{U_\infty \delta_o}{\nu}$ is the Reynolds number based on the free-stream velocity U_∞ and a reference boundary-layer thickness δ_o. In most previous numerical approaches, the vorticity transport equation is numerically solved in conjunction with an equivalent stream function representation of equations (1) and (2). Such a stream function, vorticity solution field then allows for the calculation of the equivalent velocity and pressure fields. In the present paper, the differential forms, equations (1) to (3), are discretized directly and thus provide a velocity-vorticity description of the flow. Since the details of the discretization and the algorithm appear in Ref. 9, we only present the discretized form of the equations, for completeness, and the various extensions and enhancements unique to the present problem.

Since the present formulation can be expressed in Cartesian coordinates, consider the computational cell depicted in Fig. 2 with the associated distribution of dependent variables about the cell. As mentioned earlier, a

variable associated with the side of a cell is interpreted as the average of that variable over the side of the cell and one associated with the center of a cell is an average over the cell. In addition, the notation

$$\mu_x \, w^n_{j,k} = \left(w^n_{j+1/2,k} + w^n_{j-1/2,k} \right)/2 \tag{4a}$$

$$\delta_x \, w^n_{j,k} = \left(w^n_{j+1/2,k} - w^n_{j-1/2,k} \right)/\Delta x_j \tag{4b}$$

$$\nabla_x \, w^n_{j,k} = 2\left(w^n_{j,k} - w^n_{j-1,k} \right)/\left(\Delta x_j + \Delta x_{j-1}\right) \tag{4c}$$

is used for the x-direction in the following: with a completely analagous form used for the y-direction. Also, for brevity and to avoid confusion, the spatial indices will be suppressed, that is $w^n_\bullet = w\left(\Delta x_j, \, \Delta y_k, \, n \, \Delta t\right)$. In the following subsections, the velocity and vorticity solvers will be described along with the details of the solution procedure.

Velocity Difference Equations and Solver

The difference approximations to equations (1) and (2) and the auxiliary averaging conditions needed in the solution procedure are given by (Ref. 9)

$$\delta_x \, u^n_\bullet + \delta_y \, v^n_\bullet = 0 \tag{5a}$$

$$\delta_x \, v^n_\bullet - \delta_y \, u^n_\bullet = \zeta^{n-1/2}_\bullet \tag{5b}$$

$$(\mu_x - \mu_y)u^n_\bullet = 0, \quad (\mu_x - \mu_y)v^n_\bullet = 0 \tag{6a,b}$$

An iteration scheme can be applied to equations (5) and (6) for the values $U = (u,v)^T$ associated with the sides of a computational cell: the resulting algorithm is

$$U_\bullet^{(\ell+1)} = U_\bullet^{(\ell)} + \omega B^T \left(B \cdot B^T \right)^{-1} \begin{pmatrix} R_1\left(U_\bullet^{(\ell)}\right) \\ R_2\left(U_\bullet^{(\ell)}\right) \end{pmatrix} \tag{7}$$

where $U_\bullet^{(\ell)}$ is the approximation to $U_\bullet$ at the ℓth iteration,

$$B \equiv \begin{pmatrix} \lambda_\bullet I, & -\lambda_\bullet I, & C, & -C \\ I, & I, & -I, & -I \end{pmatrix}, \qquad C = \begin{pmatrix} 0 & 1 \\ -1 & 0 \end{pmatrix}, \tag{8a,b}$$

I is the 2×2 identity matrix, $\lambda_\bullet$ is the aspect ratio $\dfrac{\Delta y_k}{\Delta x_j}$ of each cell, and $\omega (=1.7)$ is an extrapolation parameter whose value is determined by numerical experiments. $R_1\left(U_\bullet^{(\ell)}\right)$ and $R_2\left(U_\bullet^{(\ell)}\right)$ are residuals defined by

$$R_1\left(U_\bullet^{(\ell)}\right) \equiv \delta_x U_\bullet^{(\ell)} + C \, \delta_y U_\bullet^{(\ell)} - (0,\varsigma)^T \tag{9a}$$

$$R_2\left(U_\bullet^{(\ell)}\right) \equiv \mu_x U_\bullet^{(\ell)} - \mu_y U_\bullet^{(\ell)} \tag{9b}$$

Thus equation (7) is analogous to an SOR-type iterative technique. At cells adjacent to the boundaries the matrix B is altered to account for the known velocity values at the edges of the bounding cells.

In the solution procedure the flow domain is divided into two regions: the region above the bounding flat plate and cavity, that is, the top region, and the cavity region itself. The coupling of the two regions in an overall solution solver will be described in the "Solution Procedure" section. For the present it will suffice to specify the boundary conditions in each region.

In the top region, the inflow u velocity is specified and is determined from the Blasius solution to the streamwise momentum equation for a given inflow boundary-layer thickness. This u velocity boundary condition is time independent. Along the flat plate the v velocity is set to zero, and along the top of the computational domain the nondimensional free-stream velocity U_∞ is set to unity. Both of these boundary conditions are also time independent. Finally, at the outflow boundary a time dependent flux condition for the v velocity is used, that is

$$v_{M,k}^n = v_{M,k}^{n-1} - \Delta t \left(u_{M,j}^{n-1} \nabla_x v_{M,j}^{n-1} - v_{M,j}^{n-1} \nabla_x u_{M,j}^{n-1} \right) \tag{10}$$

where $j + 1/2 = M$ is the location of the outflow edge of the downstream boundary cells. Note that in equation (10) the continuity equation (eq. (1)) has been utilized, while viscous and transverse pressure gradient effects have been neglected.

In the cavity region, the specification of the boundary conditions is straightforward. Along the solid boundaries of the cavity, the normal velocity components are specified. All these velocities are zero and are time independent. Along the interface with the top region of the computational domain, all velocities are required to be continuous. The details of the solution sequence at the interface is described in the "Solution Procedure" section.

Vorticity Difference Equations and Solver

The difference approximations to equation (3) and the auxiliary averaging conditions needed in the solution procedure are given by (Ref. 9)

$$\left(\delta_t + \hat{u}^n_\bullet \, \delta_x + \hat{v}^n_\bullet \, \delta_y\right)\zeta^n_\bullet = \frac{1}{R}\left(\delta_x \, \phi^n_\bullet + \delta_y \, \psi^n_\bullet\right) \tag{11}$$

with

$$\mu_t \, \zeta^n_\bullet = \mu_x \, \zeta^n_\bullet = \mu_y \, \zeta^n_\bullet \tag{12a}$$

$$\delta_x \, \zeta^n_\bullet = \left(\mu_x - \frac{1}{2}\,\Delta x_j \, q_x \, \delta_x\right)\phi^n_\bullet \tag{12b}$$

$$\delta_y \, \zeta^n_\bullet = \left(\mu_y - \frac{1}{2}\,\Delta y_k \, q_y \, \delta_y\right)\psi^n_\bullet \tag{12c}$$

where

$$\hat{u}^n_\bullet = \mu_x \, u^n_\bullet \,, \qquad \hat{v}^n_\bullet = \mu_y \, v^n_\bullet$$

$$q_x = q(\theta_x) = \coth\theta_x - \theta_x^{-1} \,, \quad q_y = q(\theta_y) = \coth\theta_y - \theta_y^{-1}$$

$$\theta_x = \frac{u_\bullet \, \Delta x_j \, R}{2} \,, \qquad \theta_y = \frac{v_\bullet \, \Delta y_k \, R}{2} \tag{12d}$$

As shown in Ref. 9, this system of equations, and the corresponding ADI approximations, can be solved by repeated use of a tridiagonal system of equations. For example, in the x-direction the ζ^n variables associated with the sides of each cell are determined from

$$\frac{1}{2}\left[(1 - q_x)(1 + \lambda_x \, \hat{u}^n_\bullet) - K_x\right]\zeta^n_{j+1,k}$$

$$+\,\frac{1}{2}\left[(1 + q_x)(1 - \lambda_x \, \hat{u}^n_\bullet) - K_x\right]\zeta^n_{j-1,k}$$

$$+\,\left[1 + \lambda_x \, \hat{u}^n_\bullet \, q_x + K_x\right]\zeta^n_{j,k}$$

$$= (1 - q_x)\, g^n_{j+1/2,k} + (1 + q_x)\, g^n_{j-1/2,k} \tag{13}$$

where $\lambda_x = \dfrac{\Delta t}{\Delta x_j}$, $K_x = \dfrac{2 \, \Delta t}{R \, \Delta x_j^2}$, and the function $g_\bullet^n$ are described in Ref. 9. Note that the index $j = 1, 2, \ldots, M-1$ varies over the range of cells in the x-direction and that at each cell the coefficient values differ due to the dependence on grid size. The corresponding function $\phi_\bullet^n$ can be obtained from the vorticity values obtained in equation (13) by solving

$$\phi_\bullet^n = \frac{R}{4} \left[(q_x - 1)(1 + \lambda_x \, \hat{u}_\bullet^n) + K_x \right] \zeta_{j+1,k}^n$$

$$+ 2 \left[q_x + \lambda_x \, \hat{u}_\bullet^n \right] \zeta_{j,k}^n + \left[(q_x + 1)(1 - \lambda_x \, \hat{u}_\bullet^n) - K_x \right] \zeta_{j-1,k}^n$$

$$+ 2(1 - q_x) \, g_{j+1/2,k}^n - 2(1 + q_x) \, g_{j-1/2,k}^n \tag{14}$$

With the solution of equations (13) and (14), the solution set (ζ^n, ϕ^n) are known throughout the field; and with the solution of a completely analogous set of equations for the y-direction, the solution set (ζ^n, ψ^n) will be known throughout the field. Once the variables $(\zeta^n, \phi^n, \psi^n)$ are known at time level n, it is a simple step to directly impose either equation (11) or equation (12) and obtain $\zeta_\bullet^{n+1/2}$ for the entire flow field.

The remaining issue to be addressed is the choice of boundary conditions for the vorticity. Due to the tridiagonal formulation, it is not necessary in the vorticity solver to solve the equations in the top and cavity region separately, but to simply solve for the vorticity edge values by successive sweeps over the range of x and y values. Thus, in the x-direction the sweep goes from the inflow boundary to the outflow boundary, and in the y-direction from the flat plate or bottom of the cavity to the top of the computational domain. At the inflow boundary, the vorticity values are deter-

mined from the Blasius solution and are held fixed for all time. Along the flat plate and cavity solid boundaries, the vorticity is determined from second order accurate one-sided difference approximation to the appropriate nonzero velocity derivative. Finally, along the top and outflow boundaries, vorticity flux conditions are applied. For example, the flux condition applied at the outflow boundary is derived from the vorticity transport difference equation and is written as

$$
\zeta^n_{M,k} = - \zeta^n_{M-1,k} + 2.0\ \zeta^{n-1/2}_\bullet
$$

$$
- \Delta t \left(\hat{u}^n_\bullet\ \nabla_x\ \zeta^{n-1/2}_\bullet + \hat{v}^n_\bullet\ \nabla_y\ \zeta^{n-1/2}_\bullet \right) \tag{15}
$$

where $j = M - 1/2$, k is the center of an outflow boundary cell. A completely analogous equation is used for determining the vorticity boundary values at the free-stream boundary at the top of the computational domain.

Solution Procedure

The time-dependent solution for flow over the embedded cavity was obtained by first solving the equations for the flow over a flat plate and then using the flat plate solution field as initial conditions for the flow over an embedded cavity. The computational domain for the flat plate case was the same as the corresponding embedded cavity case except that the top of the cavity was replaced by a solid surface. All grid spacings in both cases were the same.

First, a description of the solution procedure for the flat plate case will be given. In all test cases presented, the initial values used

throughout the flow domain were the appropriately averaged inflow Blasius velocity and vorticity fields. This initial set of field values is in error since it does not account for the boundary-layer growth in the streamwise direction and, even if boundary-layer growth were accounted for, the Blasius solution is not a solution to the full Navier-Stokes equations.

The solution procedure begins by entering the velocity solver, described in the "Velocity Difference Equation and Solver" section, and iterating the solution set obtained from equation (7) until the convergence criteria

$$\max \left(R_1(U_\bullet^{(\ell)}), \ R_2(U_\bullet^{(\ell)}) \right) < \min_{j,k} \left(\Delta x_j^2, \ \Delta y_k^2 \right) \qquad (16)$$

are met. When these criteria are met, the velocity values at time level n are known. From these velocity values, the requisite vorticity boundary values at time level n are determined using second order accurate one-sided differences.

With the velocity field at time level n known, the vorticity field at time level n is required. As outlined in the "Vorticity Difference Equations and Solver" section, the solution procedure is a straightforward implementation of equations (11) through (13), and the corresponding equations for the y-direction, using the prescribed vorticity boundary conditions (Ref. 9). Once the vorticity values and their derivatives at the edges of the computational cells and at time level n are known, it is necessary to obtain the vorticity values associated with the center of each cell at time level $n + 1/2$. This is done by solving the vorticity transport equation (eq. (11)), or implementing the averaging condition equation (eq. (12a)). The solution procedure then continues onto the velocity solver with the vorticity values $\zeta_\bullet^{n+1/2}$ as new input forcing functions.

The entire solution sequence continues until the number of iterations in the velocity solver falls to $\ell < 3$, and the velocity and vorticity L_2 norms, that is the energy and enstrophy, become time independent. A schematic representation of the solution sequence is shown in Fig. 3.

With the establishment of the flat plate solution, the computed velocity and vorticity values are used as input in the embedded cavity problem. The cavity domain is initially filled with zero values for both the velocity and vorticity.

In the velocity solver a two-step procedure is used: first, the cavity field is swept and the common velocity values at the interface between the cavity domain and top domain are equated; second, the top domain is swept using the boundary conditions and interface velocity values. The maximum residuals from both the cavity and top are compared with the convergence criteria, equation (16). The process is repeated through both the cavity and top computational domains until the convergence criteria are met. Once this occurs, the velocity field for the entire domain is known at time level n; and, in addition, the vorticity values along the solid boundaries are also known at time level n.

The vorticity solution sequence is not altered by the presence of the cavity. The solution values are determined by sequential sweeps in both the streamwise and transverse directions. When the sweep is in the x-direction, it is either from the inflow boundary to the outflow boundary in the top or from the left wall to the right wall in the cavity. When the sweep is in the y-direction, it is either from the flat plate to the top of the computational domain or from the bottom of the cavity to the top of the computational domain. This procedure yields ζ^n, ϕ^n, and ψ^n values for the entire domain. Finally, the $\zeta^{n+1/2}$ vorticity values at the center of the

computational cells for both the top and cavity domains are determined from either equation (11) or (12a).

From the results of the computations, it appears that even with the embedded cavities the flow does reach a state of dynamic equilibrium. Thus, the computational procedure continues for the flow over an embedded cavity until the termination criteria of $\ell < 3$ and time independent L_2 norms are met.

RESULTS AND DISCUSSION

As mentioned in the Introduction, one of the purposes of this study is to isolate the important dynamic characteristics of the flow over an embedded cavity. In the present work the flow above the cavity is laminar and is used as an aid in sorting out the physics of the turbulent case. In the turbulent case, the presence of vortical structures in the vicinity of the wall can cause significant alteration of the dynamics in the vicinity of the cavity. Unfortunately, it is difficult to delineate the overriding dynamic process, or processes, since the boundary turbulent flow encompasses a broad spectrum of dynamically relevant scales. A similar motivation prompted the experimental study in Ref. 3, where it was determined that the strong random massexchange activity observed in cavities with bounding turbulent flow was due to excitation from the turbulent fluctuations rather than an instability of the cavity flow itself. With the present numerical study, a more detailed analysis of the relevant dynamic variables can be performed. For example, as will be shown later in this section, the flow relaxation length upstream and downstream of the various cavities examined can be determined. This can be used to optimize the relative spacing between transverse rows of cavities to enhance the drag reducing characteristics of such flows.

The results presented were compiled from four test cases. All cavities were square and ranged from 0.25 to 1.00 boundary-layer thicknesses deep. In order to establish the relevant base parameters from which the calculations could be run, the experimental study of Ref. 5 was used as a guide. This was done to insure that over the range of parameters studied the flow in the vicinity of the cavity could be characterized as laminar separating flow and that within this computational range the flow neither became transitional nor turbulent. The reference boundary-layer thickness was determined from a Blasius solution of the streamwise momentum equation at a dimensional distance of $x = 80$ cm from the leading edge of the flat plate and a corresponding free-stream velocity of 120 cm/sec. The boundary-layer thickness was $\delta_o = 1.68$ cm and the reference Reynolds number, $R = \dfrac{U_\infty \delta_o}{\nu}$, was 1188.

The flow domain was discretized into a nonuniform set of Cartesian grid cells in the top boundary-layer region and a set of uniform grid cells in the cavity. The minimum and maximum nondimensional grid cell sizes ranged from 0.0125 to 0.8, respectively. The largest were placed away from regions of dynamic significance. The grid cell distribution in the cavity ranged from 10×10 cells in the smallest cavity to 40×40 cells in the largest cavity. In the case of the smallest cavity, the number of grid cells in the cavity was increased to 20×20 to insure the accuracy of the results with the coarser grid. In the top region, the number of grid cells in the vertical direction was held fixed at 40 and the number of grid cells in the streamwise direction ranged from 70 in the small cavity case to 90 in the large cavity case. In all cases the ratio of lengths in a given direction in adjacent cells never exceeded 2. The free-stream boundary was located approximately 5 boundary-layer thicknesses above the flat plate; and the inflow and outflow boundaries were placed approximately 2.5 and 5 boundary-layer thicknesses

upstream and downstream of the cavity, respectively. In all cases pressure contour plots were used to confirm that none of the computational boundaries interferes with the physical results in the vicinity of the cavity.

Figure 4 shows stream function contours in the vicinity of the cavity. It must be noted that in this figure and subsequent figures where the cavities are sketched, the physical size of the cavities differ; however, for presentation purposes, the cavity sizes in the figures have been normalized. In addition, in all the contour plots presented the dashed lines represent contours with negative values and solid lines represent contours with positive values. As can be seen, a strong recirculation region characterizes the cavity flow over most of the cavity. This causes the flow in the vicinity of the interface with the outer boundary flow to be accelerated locally; that is, a favorable pressure gradient is induced locally by the presence of the cavity. This effect is depicted by the convex curvature of the bounding streamline at the mouth of the cavity. Note that the bounding streamline, which has a value of 10^{-4} in all cases presented, is located at differing distances from the flat plate bounding surface. This is due to the fact that, as indicated earlier, the different physically sized cavities have been normalized for presentation purposes. As the cavities deepen, although they remain square, the recirculation region begins to be skewed to the downstream side of the cavity. This increases the curvature of the bounding streamline pattern, thus causing a more favorable local pressure gradient and a stronger local flow acceleration. In addition, the bounding streamline pattern in all the cases indicates that the flow is locally accelerated at both the upstream and downstream corners.

In conjunction with the stream function contours the local velocity profiles can be examined. Figure 5 shows the variation of the streamwise

velocity profiles at various stations in the cavity. The figure indicates a relatively low level of streamwise momentum in the cavity: however, as the cavity's size is increased, stronger backflow begins to become evident near the downstream side of the cavity. This shear layer thickening is caused by the recirculation region becoming skewed in the downstream direction. It could be anticipated that as the recirculation region grew the shear layer thickening would become evident closer to the upstream side of the cavity. It should be noted at this point that in the Reynolds number and cavity sizes studied no laminar flow instabilities arose in this bounding shear layer. Since this was a time dependent numerical study incorporating the full form of the vorticity transport equation, any interfacial instabilities, either spatial or temporal, would be easily detected in the streamline or velocity plots. An examination of these plots, or the vorticity contour plots to be presented next, showed no indication of interfacial instabilities. This observation is in agreement with Ref. 3 where no laminar oscillations occurred below a cavity Reynolds number, $\frac{U_\infty d}{\nu}$, of 2400. In the present study, the maximum cavity Reynolds number is approximately 1400.

The iso-vorticity contours in Fig. 6 show that as the cavity size increases the vortex in the cavity is, indeed, skewed to the downstream side of the cavity. This downstream shift causes a thickening of the shear layer on this side of the cavity. Note that this asymmetry of vorticity in the vortical recirculation region must also cause a corresponding increase of vorticity, of opposite sign, in the immediate vicinity of the downstream wall of the cavity as well. A consequence of this is the strengthening of the relatively weak vortex region present in the lower right-hand corner of the cavity. This is due to the fact that fluid is accelerated downward by the action of the two counterrotating vortical regions at the top of the cavity

and this accelerated fluid causes the strengthening of the rotational motion at the bottom of the cavity. Note that the stream function contours did not indicate the presence of the recirculation regions at the bottom of the cavities. This was due to the fact that the vorticity is a more sensitive measure of such flow dynamics and to include such motion into a streamline representation would have required an unnecessary significant increase in the number of streamline contours. Finally, it can be concluded that in the temporal development of the embedded cavity flow, the vortex in the lower downstream corner of the cavity must be developed before the vortex in the lower upstream corner of the cavity. This leads to the speculation that if the downstream vortex is precluded from forming, by either flow suction or some other means, then the upstream vortex may also be inhibited.

One of the main objectives of the present study was to examine the effects of the embedded cavity on total drag. In the absence of the cavity the drag is due solely to skin friction; with the cavity, the effects of pressure drag on the vertical walls of the cavity must be accounted for in addition to friction drag. A comparison of integrated C_D/C_F between the flat plate with cavity and the flat plate is shown in Fig. 7 as a function of the nondimensional streamwise coordinate x. Upstream of the cavity there is very little difference between the two cases, although there is a slight increase near the upstream corner of the cavity in all cases. Along the upstream vertical wall the pressure thrust is such as to cause a local drag reduction; and along the downstream vertical wall the pressure drag is such as to cause a local drag increase. Note that pressure drag increase on the downstream vertical wall is larger than the pressure drag decrease on the upstream vertical wall. In addition, the frictional drag on the bottom of the cavity is significantly lower than the reference frictional drag on the

corresponding flat plate in the absence of the cavity. This, of course, is due to the insignificant induced motion on the bottom of the cavity. In fact, if these were the only additional induced forces due to the presence of the cavity, the net drag reduction would be approximately 3%, 5%, 9%, and 7%, respectively, for the range of shallow to deep cavities studied. Unfortunately, there is another dynamic process involved which causes an additional increase in drag. Even in the laminar flow case studied here there are stress relaxation effects present in the flow. As can be seen in Fig. 7, these frictional forces cause the total drag to eventually relax back to the flat plate boundary-layer case. Thus, in the present study the embedded cavities do not appreciably alter the drag characteristics of the flow. This is in agreement with the laminar behavior of rough walls as documented in Ref. 11.

Even in light of the benign effect of the embedded cavities, it is of interest to analyze in some detail the various contributing forces to the total drag. In Fig. 8 are depicted the variation of C_p on the upstream and downstream vertical walls of the cavity as well as on the bottom of the cavity. As is shown, only near the top of the cavity at the upstream corner do pressure forces act to reduce the overall drag. In the remaining portions of the vertical walls, pressure forces add to the net drag. It is also of interest to note in this figure that the pressure is relatively uniform over a large portion of the cavity and that any significant pressure thrust or pressure drag occur in the upper portions of the cavity near the corners.

Finally, it is necessary to examine the remaining contributor to the total drag, that is, the drag due to the stress overshoots upstream and downstream of the cavity. In Fig. 9 the variation of the wall shear stress,

$\tau_w = \frac{1}{R} \frac{\partial u}{\partial y}\bigg|_w$, with downstream location is shown. The stress overshoot regions,

relative to the flat plate case, are clearly depicted in the figure. Note that the flat plate wall shear is indicated by the dashed line which, of course, is a decreasing function of the streamwise distance x. In all cases, the magnitudes of the overshoots are quite similar; however, the relaxation distances tend to increase with the size of the cavity. This suggests that a maximum separation distance exists, beyond which the cavities act independently and no net drag reduction occurs. If the cavities are placed within the relaxation distance it may be possible to effectively couple the sequential cavities and achieve some net drag reduction. This type of placement is further indicated by the drag due to the stress relaxation. For example, in the four cases examined, the drag increase due to the stress overshoots is about 35% of the frictional drag decrease due to the presence of the cavity. Thus, if some means of minimizing the overshoots could be found, either by optimal spacing of sequential cavities or optimal design of the cavities themselves, then some net drag reduction might be realized.

Table I summarizes the component drag contributions from the pressure forces and frictional forces. In all cases the comparisons are made up to the end of the stress relaxation region downstream of the cavity. As is shown, the net reduction in drag, relative to the flat plate case, is insignificant for the cases studied in this work. Nevertheless, in the deepest cavity case, the reduction, even though small, is less than in the d = 1/2 and d = 3/4 cases. Whether this is the beginning of a trend toward increased drag for deeper cavities is not clear, and must, for the time being, remain as a subject for future study.

Finally, the fact that the flow in the vicinity of the cavity has a smaller momentum thickness than that of the flow on a flat plate suggest that a cavity may have a positive effect on a separating flow. The usual physical

description of separation is that an adverse pressure gradient causes the deceleration of the low momentum flow near the surface. The results in this paper show that the cavity creates, in effect, a locally favorable pressure gradient. It therefore appears that the introduction of a cavity at, or just forward of, the separation point on a body might shift the separation point downstream. Such a conjecture is substantiated by the results in Ref. 12 where circumferential grooves were used to delay separation and reduce drag on an axisymmetric bluff-body. The detailed flow structure about a cavity placed in the vicinity of a separation point can be studied by the method described in this paper, and initial calculations on such flows are in progress.

Conclusions

From the results presented in this section, a clear picture of the flow in the vicinity of the cavity emerges. The presence of the cavity causes an upstream as well as downstream modification of the flow, as was seen from the variation of wall shear stress with position in Fig. 9. From these results, it can be seen that, in all cases, the upstream influence extends for a distance equal to about 0.25 of a boundary-layer thickness. Downstream of the cavity the region of cavity influence increases with increasing cavity size. The length of this region changes from about 1 boundary-layer thickness for the smallest cavity to about 1.75 boundary-layer thicknesses for the largest cavity. Upstream of the cavity there is, effectively, a favorable pressure gradient; the boundary-layer thickness decreases and the shear stress increases. The flow accelerates across the cavity and, on the downstream edge of the cavity the shear stress is very high, reaching approximately twice that of the zero pressure gradient Blasius boundary layer. Thus, for the range of

cavity sizes studied, it can be concluded that cavities which are approximately 2 to 3 boundary-layer thicknesses apart can be treated as if they were isolated. An interesting question arises as to what the flow characteristics are for closely spaced cavities, those separated by a boundary-layer thickness or less.

Finally, as mentioned at the end of the last section, the results of this study can be extrapolated to suggest that the placement of a cavity in the vicinity of a separation point can delay separation.

Acknowledgement

References

1. Roshko, A.: Some Measurements of Flow in a Rectangular Cutout. NACA TM-3488, August 1955.

2. Tani, S.; Suchi, M.: Komodo, M.: Experimental Investigation of Flow Separation Associated with a Step or a Groove. Aeronautical Research Institute, University of Tokyo, Report No. 364, April 1961.

3. Reihman, T.: Laminar Flow Over Transverse Rectangular Cavities. University Microfilms, Publication No. 67-17,072, Ann Arbor, Michigan, Ph.D. Thesis, California Institute of Technology, 1967.

4. Sarohia, V.: Experimental Investigation of Oscillations in Flows Over Shallow Cavities. AIAA Journal, Vol. 15, 1977, pp. 984-991.

5. Sinha, S. N.; Gupta, A. K.; Oberai, M. M.: Laminar Separating Flow Over Backsteps and Cavities, Part II. Cavities. AIAA Journal, Vol. 20, 1982, pp. 370-375.

6. Rockwell, D.; and Knisely, C.: The Organized Nature of Flow Impingement Upon a Corner. Journal of Fluid Mechanics, Vol. 93, Pt. 3, 1979, pp. 413-432.

7. Borland, C. J.: Numerical Prediction of the Unsteady Flowfield in an Open Cavity. AIAA 10th Fluid and Plasma Dynamics Conference, Albuquerque, New Mexico, June 27-29, 1977, Paper No. 77-673.

8. Hankey, W. L.; and Shang, J. S.: The Numerical Solution to Pressure Oscillations in an Open Cavity. AIAA 17th Aerospace Sciences Meeting, New Orleans, Lousiana, January 15-17, 1979, Paper No. 79-0136.

9. Gatski, T. B.; Grosch, C. E.; and Rose, M. E.: A Numerical Study of the Two-Dimensional Navier-Stokes Equations in Vorticity-Velocity Variables. Journal of Computational Physics, Vol. 98, No. 1, October 1982, pp. 1-22.

10. McInville, R. M.; Gatski, T. B.; and Hassan, H. A.: Embedded Shear Layer Computations for Increased Drag Reduction. AIAA 22nd Aerospace Sciences Meeting, January 9-12, 1984, AIAA Paper No. 84-0349.

11. Mills, A. F.; and Courtney, J. F.: Turbulent Boundary Layers on Rough Walls. March 1976, AFOSR-TR-76-1098.

12. Howard, F. G.; Goodman, W. T.; Walsh, M. J.: Axisymmetric Bluff-Body Drag Reduction Using Circumferential Grooves. AIAA Applied Aerodynamics Conference, Danvers, Massachusetts, July 13-15, 1983, AIAA Paper No. 83-1788.

Table I.- Distribution of Drag Forces and Percent Drag Reduction

Cavity size	Pressure drag ($\times 10^{-4}$)	Differential friction drag[a] ($\times 10^{-4}$)	Total differential drag[b] ($\times 10^{-4}$)	Percent reduction[c]
$\ell = d = \frac{1}{4}$	1.4	-2.0	-0.6	-0.9
$\ell = d = \frac{1}{2}$	3.3	-4.2	-0.9	-1.3
$\ell = d = \frac{3}{4}$	4.9	-6.8	-1.9	-2.4
$\ell = d = 1$	7.5	-8.7	-1.2	-1.5

[a]Frictional drag with cavity minus frictional drag without cavity.
[b]Pressure drag plus differential frictional drag.
[c]Total differential drag divided by frictional drag on flat plate.

Figure Captions

Fig. 1   Cavity embedded in laminar boundary-layer flow.

Fig. 2   Dependent variable distribution in a computational cell.

Fig. 3   Schematic of solution procedure.

Fig. 4   Stream function contours. Contour levels: (a) -0.0006 to 0.0035;
(b) -0.0025 to 0.018; (c) -0.005 to 0.012; (d) -0.007 to 0.012.

Fig. 5   Streamwise velocity profiles in and near cavity.   Profiles drawn in
cavity are equi-spaced over length of cavity ℓ.

Fig. 6   Iso-vorticity contours.   Contour levels: (a) -3.20 to 0.60;
(b) -2.80 to 1.00;   c) -3.20 to 1.40;   d) -3.20 to 1.40.

Fig. 7 C_d/C_f as a function of streamwise distance x: (a) $\ell = d = \frac{1}{4}$;
(b) $\ell = d = \frac{1}{2}$; (c) $\ell = d = \frac{3}{4}$; (d) $\ell = d = 1$.

Fig. 8 C_p along walls and floor of cavity: (a) $\ell = d = \frac{1}{4}$; (b) $\ell = d = \frac{1}{2}$;
(c) $\ell = d = \frac{3}{4}$; (d) $\ell = d = 1$.

Fig. 9   Wall shear stress as a function of streamwise distance x:
(a) $\ell = d = \frac{1}{4}$; (b) $\ell = d = \frac{1}{2}$; (c) $\ell = d = \frac{3}{4}$; (d) $\ell = d = 1$.
Flat plate reference case

Figure 1

$$\underline{u}^n_{i,j+\frac{1}{2}}; \quad \zeta^n_{i,j+\frac{1}{2}}; \quad \psi^n_{i,j+\frac{1}{2}}$$

$$\underline{u}^n_{i-\frac{1}{2},j}; \quad \zeta^n_{i-\frac{1}{2},j}; \quad \phi^n_{i-\frac{1}{2},j} \qquad \zeta^{n\pm\frac{1}{2}}_{i,j} \qquad \underline{u}^n_{i+\frac{1}{2},j}; \quad \zeta^n_{i+\frac{1}{2},j}; \quad \phi^n_{i+\frac{1}{2},j}$$

$$\underline{u}^n_{i,j-\frac{1}{2}}; \quad \zeta^n_{i,j-\frac{1}{2}}; \quad \psi^n_{i,j-\frac{1}{2}}$$

Figure 2

Figure 3

(4a)

(4b)

(4c)

(4d)
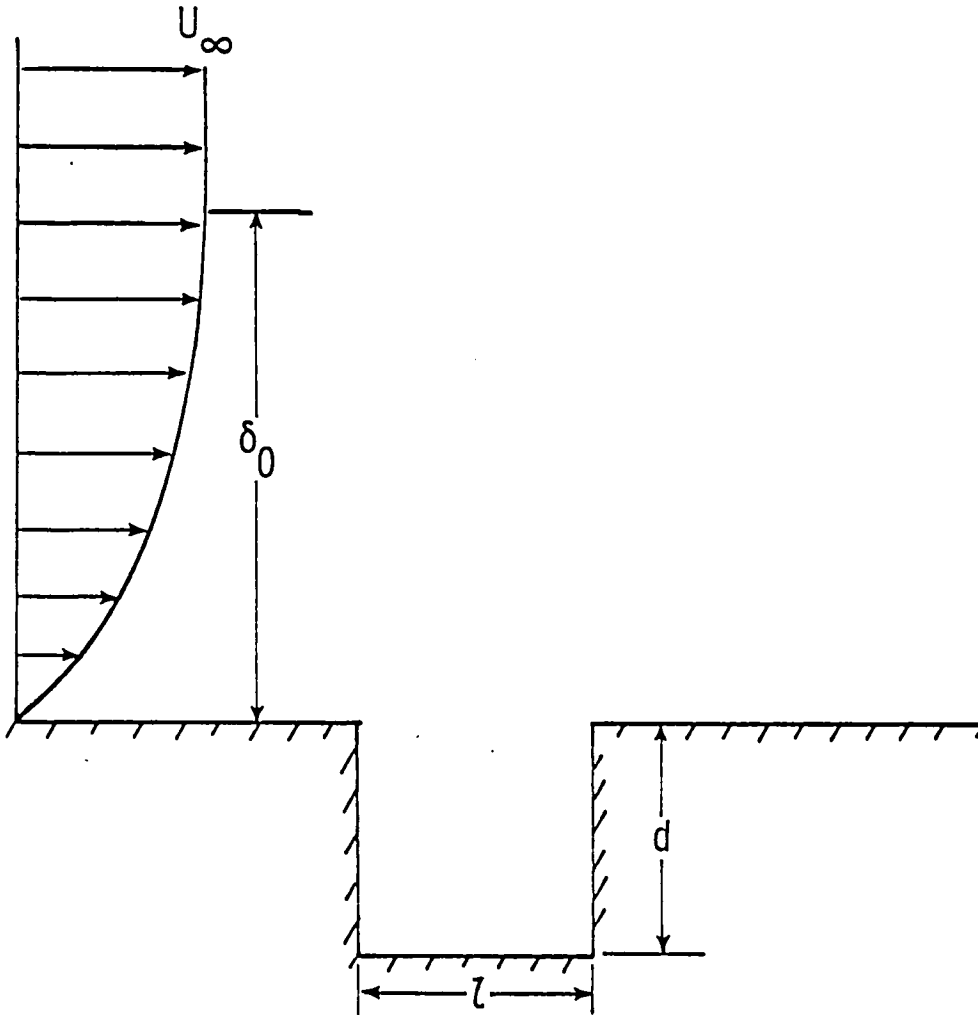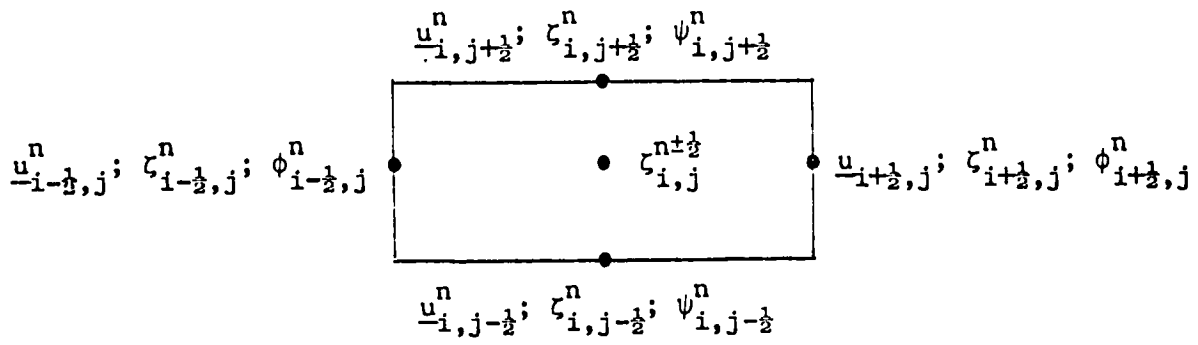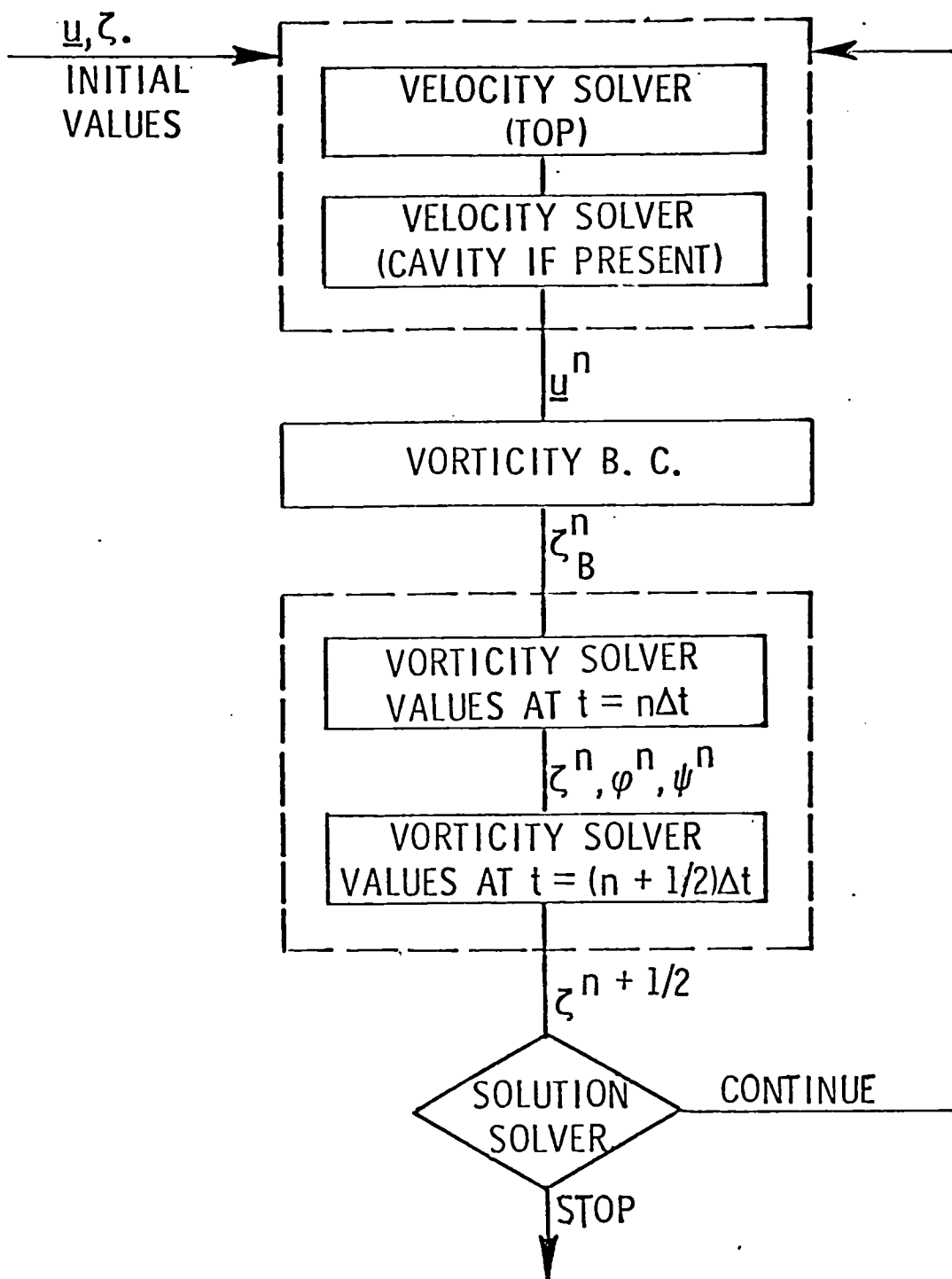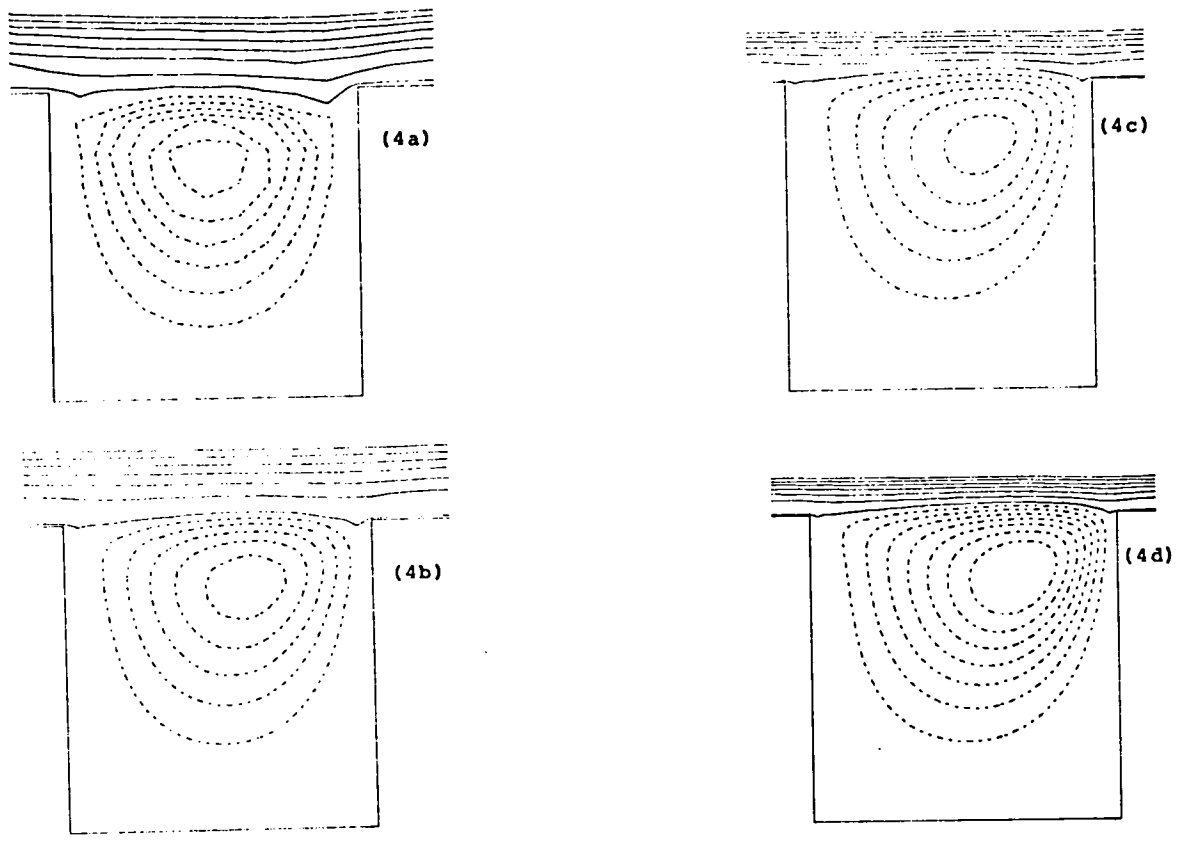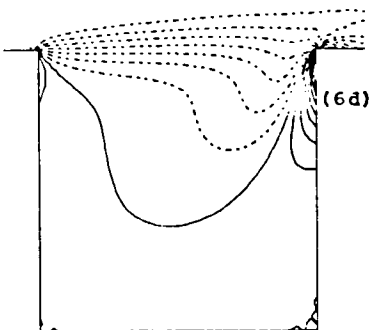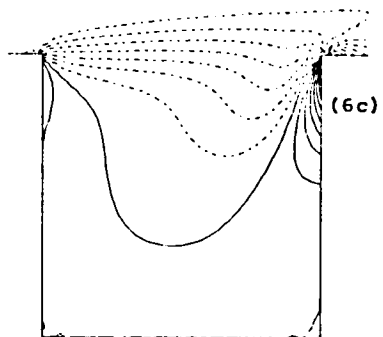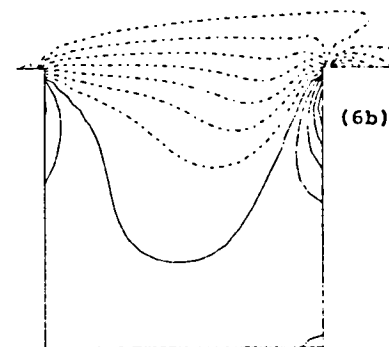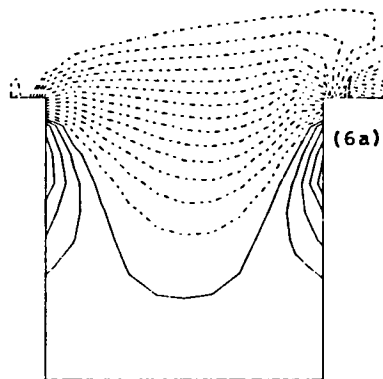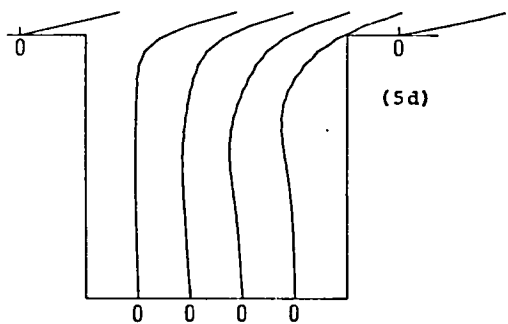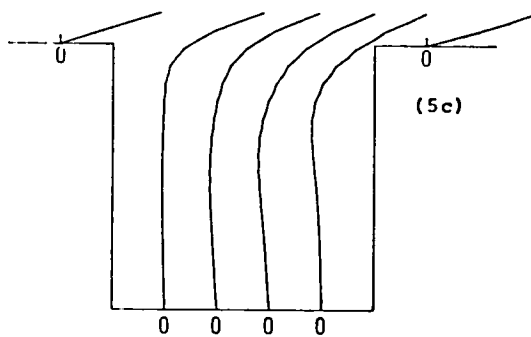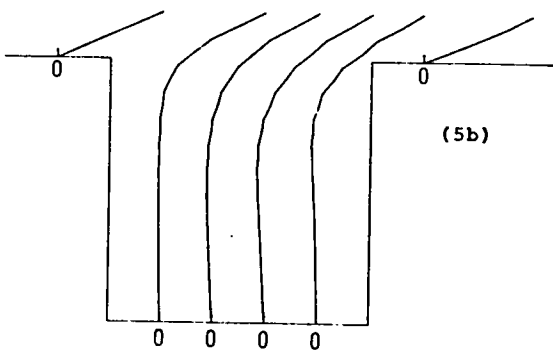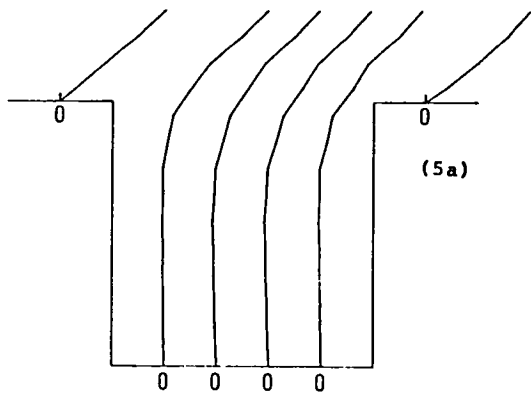
Figure 4
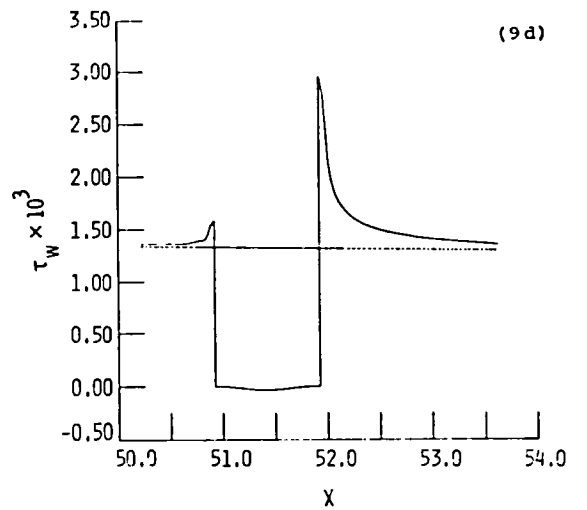
Figure 5

Figure 6
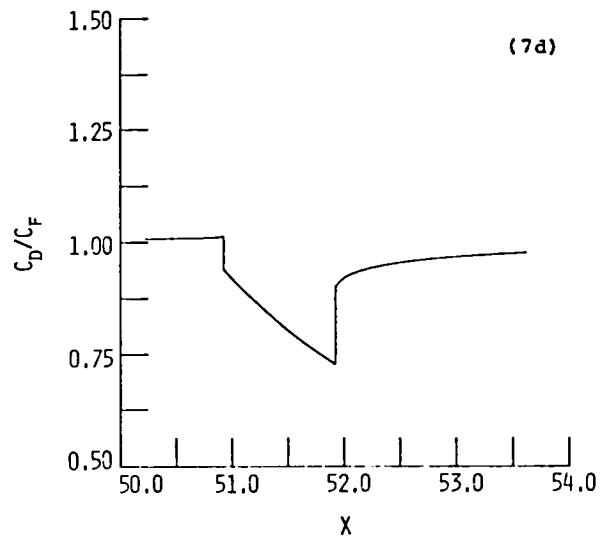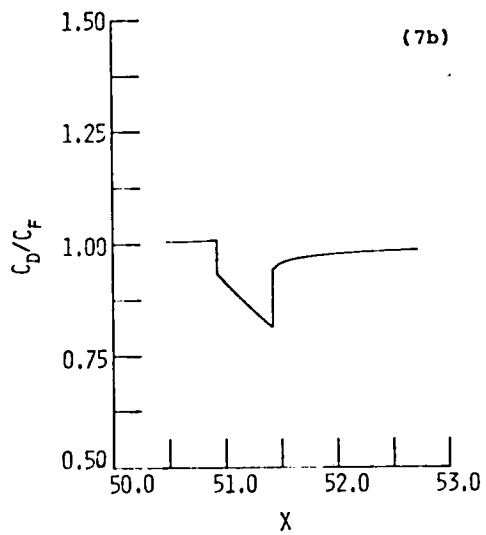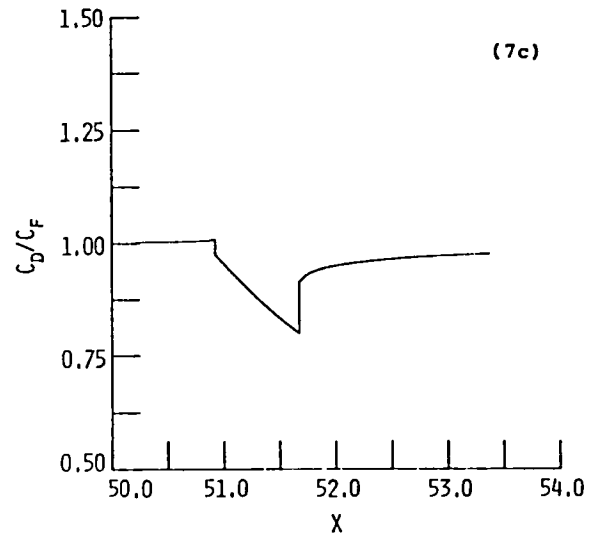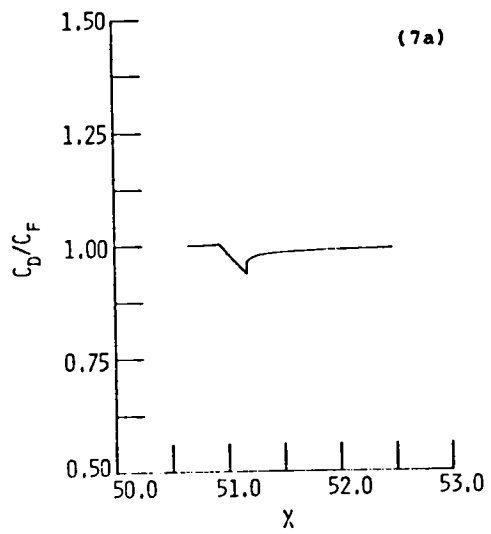
Figure 7

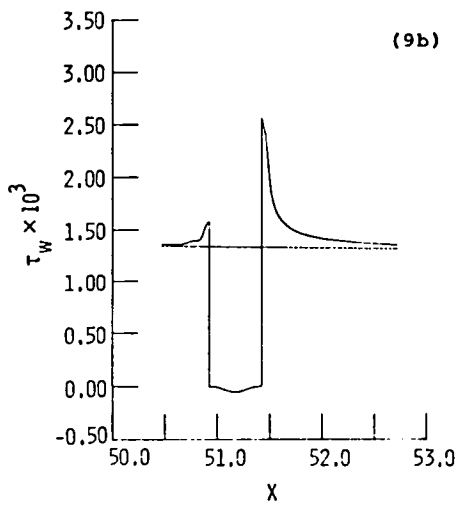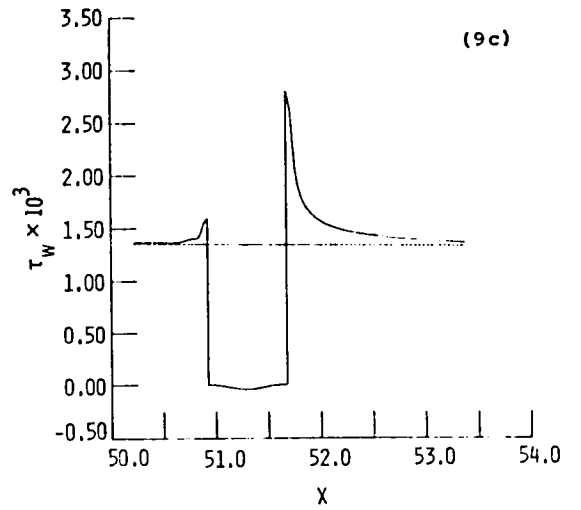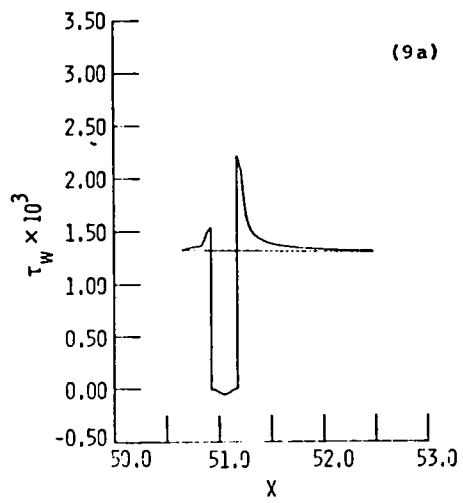**Figure 8**

Figure 9

1. Report No. NASA CR-172275	2. Government Accession No.	3. Recipient's Catalog No.
4. Title and Subtitle Embedded Cavity Drag in Steady and Unsteady Flows		5. Report Date December 1983
		6. Performing Organization Code
7. Author(s) T. B. Gatski and C. E. Grosch		8. Performing Organization Report No. 83-65
		10. Work Unit No.
9. Performing Organization Name and Address Institute for Computer Applications in Science and Engineering Mail Stop 132C, NASA Langley Research Center Hampton, VA 23665		11. Contract or Grant No. NAS1-17130
		13. Type of Report and Period Covered contractor report
12. Sponsoring Agency Name and Address National Aeronautics and Space Administration Washington, D.C. 20546		
		14. Sponsoring Agency Code

15. Supplementary Notes
Langley Technical Monitor: Robert H. Tolson   Final Report

16. Abstract

The numerical solution of the laminar boundary-layer flow over an embedded cavity is studied. The purpose of the study is to examine the relevant drag characteristics of laminar cavity flow. The solution field is obtained in terms of velocity and vorticity variables, with the stream function and pressure derivable from the directly computed variables. An analysis and comparison is made among four square cavities, ranging in size from 0.25 to 1.00 boundary-layer thicknesses deep. The dominant flow features are examined in the vicinity of the cavity by means of the stream function and iso-vorticity contours. The dominant physics in the overall drag characteristics of the flow is examined by an analysis of the pressure and wall shear stress distributions in the cavity, and upstream and downstream of the cavity. Pressure forces and frictional forces in, and in the vicinity of, the cavity are determined. Streee relaxation distances, both upstream and downstream of the cavity, are calculated and analyzed. The flow dynamics of the boundary-layer flow over an embedded cavity is summarized. Finally, the relevance of the present results to the control of flow separation in such flows is discussed.

17. Key Words (Suggested by Author(s)) surface drag time dependent flow numerical simulation	18. Distribution Statement 34 Fluid Dynamics 64 Numerical Analysis Unclassified-Unlimited		
19. Security Classif. (of this report) Unclassified	20. Security Classif. (of this page) Unclassified	21. No. of Pages 34	22. Price A03